Analysis of Three-dimensional Transition Mechanisms in the Near Wake behind a Circular Cylinder

Andrey I. Aleksyuk[a,b,*], Victor Ya. Shkadov[a]

[a]*Faculty of Mechanics and Mathematics, Lomonosov Moscow State University, Moscow 119991, Russian Federation*
[b]*Water Problems Institute, Russian Academy of Sciences, Moscow 119333, Russian Federation*

Abstract

The transition to three-dimensionality in the near wake behind a circular cylinder is studied numerically. Two modes of instability are considered for the Reynolds numbers 220 (mode A) and 300 (mode B). In the linear approximation the evolution of three-dimensional perturbations in a fluid particle can be described through the action of four mechanisms: (I) stretching of the vortex lines of perturbations by the base flow; (II) shear deformations of the vortex lines of the base flow by perturbations; (III) viscous diffusion of perturbations; (IV) solid-state rotation of fluid particles. The fields of each mechanism are determined by the results of a numerical solution of the three-dimensional NavierStokes equations. An analysis of the influence of these mechanisms is carried out and the regions of growth and decay of the three-dimensional vortex structures are identified. The main destabilizing effect is related to the stretching of vortex lines of perturbations (I) and shear deformations of the base flow vorticity (II). Viscous diffusion (III) stabilizes the flow and solid-state rotation (IV) does not influence the amplitude of perturbation in a fluid particle. For mode A there are two stages of perturbations growth: inside the elliptic part of the forming vortex and in the hyperbolic region of the braid shear layer, where the forming vortex is separated from the cylinder. At both stages the growth of three-dimensional vortex structures is mostly related to mechanism (I), however, a significant impact of mechanism (II) on this process is observed at the first stage. The most intensive growth occurs at the second stage. Perturbations of mode B are growing outside elliptic regions and are determined by mechanism (I), the shear deformations (II) have mainly a stabilizing effect. The length of perturbation enhancement time interval was estimated: it is twice as large for mode A as for mode B.

Keywords: secondary instability, wake transition, three-dimensional wake, Navier-Stokes equations

1. Introduction

In the experimental work [1] two stages of loss of stability were identified during the transition to three-dimensionality in the wake of the cylinder, which were called modes A and B. At the Reynolds number $Re = Re_A$ ($Re = U_\infty d/\nu$, where U_∞, d and ν are the free-stream velocity, the cylinder diameter, and the kinematic viscosity) large-scale three-dimensional vortex structures of mode A arise with a wavelength of about 3–4d. At the Reynolds number $Re = Re_B$ ($Re_B > Re_A$) small-scale structures of the B mode emerge with a wavelength of about 1d and three-dimensional patterns that are fundamentally different from mode A are formed. Analysis of the stability of a two-dimensional periodic flow with the application of the linear Floquet theory gives values for the critical Reynolds number and spanwise wavelength: $Re_A = 188.5\pm1$, $Re_B = 259\pm2$ and $\lambda_A = 3.96 \pm 0.02$, $\lambda_B = 0.822 \pm 0.007$ [2]. These results are in good agreement with the experiment (the value

of Re_B is higher, but this is explained by the fact that mode B in the experiment does not develop from the two-dimensional flow, but it develops together with the perturbations of mode A).

The present paper addresses the problem, which was stated among other outstanding questions in the conclusion of an extensive review [3], and the solution to it is still not completely clear: "... can we explain, with precision, the origin of mode A and B instabilities?". There are various speculations about the mechanisms of the emergence of modes A and B [4–10], but none of them is so far justified enough to become generally accepted. In particular, the most common and reasonable hypothesis about the physical mechanism of transition to a three-dimensional flow in the wake behind a cylinder (mode A formation) is the hypothesis of an elliptical instability of the vortex cores [4, 6, 7]. The structures observed in the formation of the vortices and the motion of the shed vortices in the wake strongly resemble the idealized flow generated by the elliptical instability [11]. The intensive growth of perturbations inside the hyperbolic braid region of the flow, where the main vortices are tearing from the cylinder, is considered as a secondary effect (see argumentation in [7], and for the wake of a flat plate in [12]). However, it is still

---
*Corresponding author.
  Email addresses: aleksyuk@mech.math.msu.su
(Andrey I. Aleksyuk), shkadov@mech.math.msu.su (Victor Ya. Shkadov)

not obvious that elliptic instability triggers the transition to three-dimensionality when Re exceeds the critical value Re_A. One can suggest that elliptical instability of the flow is induced by the instability of the local hyperbolic flow region downstream, where the perturbations grow intensively. Another possibility is that the presence of several mechanisms is significant in the process of transition to three-dimensionality.

In later studies, attempts have been made to localize regions that cause three-dimensional instability of the flow. In [13] it is shown that for modes A and B the process of development of three-dimensional perturbations in the near wake is slightly sensitive to the downstream three-dimensional flow in the shed vortices. Thus, it is possible to reject the hypothesis that the transition is induced by fully shed vortices. It is also shown that one cannot neglect the impact of the near wake region where vortices are formed (including the region of intensive perturbations growth mentioned above). It follows then that the hyperbolic flow region has significant influence on the formation of a three-dimensional flow in the wake. In [10] the regions causing three-dimensional instability were localized using structural sensitivity analysis, these results are consistent with [13].

Detailed information on the processes of formation, self-sustaining of vortex structures and their development for modes A and B can be found in numerous research (see, for instance, the works mentioned above and their literature reviews). In the present article we involve these results and hypotheses in the analysis of the mechanisms affecting the growth and decay of three-dimensional perturbations in fluid particles. This is done to more deeply understand the process of development of three-dimensional perturbations, which could help to clarify physical reasons for the appearance of large-scale (mode A) and small-scale (mode B) three-dimensional structures.

In our study we consider two flow regimes for 'pure' modes A (Re = 220) and B (Re = 300) which are obtained by reducing the computational domain size along the cylinder axis (Section 3.1). These regimes are simulated based on direct numerical solution of the NavierStokes equations using the Galerkin least-squares (GLS) finite-element method on unstructured tetrahedral meshes (Section 2). Four physical mechanisms responsible for growth/decay of three-dimensional perturbations (on early stages of development) in fluid particles are distinguished (Section 3). In Section 4 the main results are given: the singled out mechanisms that determine the destabilizing effect; regions in which the growth and decay of three-dimensional perturbations for modes A and B occur; estimates of growth rates and intervals; time and zones of the most intense growth of disturbances in the wake.

2. Problem Formulation and Numerical Method

The problem of a transverse viscous flow past an infinitely long circular cylinder is considered in the Cartesian coordinate system (x_1, x_2, x_3) with the axis x_3 coinciding with the axis of the cylinder. The model of a viscous perfect gas with constant specific heats, coefficients of viscosity and thermal conductivity is used. The Navier-Stokes equations governing the fluid flow in primitive variables $Y(x, t) = (p, u_1, u_2, u_3, T)^*$ (* is transposition) can be written as

$$A_0 Y_{,t} + A_i Y_{,i} = \left(K_{ij} Y_{,j} - P_i\right)_{,i} + R. \quad (1)$$

The unknown functions of the time t and coordinates $x = (x_1, x_2, x_3)$ are the dimensionless pressure $p(x, t)$, velocity $u(x, t) = (u_1, u_2, u_3)^*$, and the temperature $T(x, t)$. The matrices A_0, A_i, K_{ij} and the vector P_i ($i, j = 1, 2, 3$) arise due to the transition from conservative variables to primitive variables pressure-velocity-temperature (explicit expressions are given in Appendix A), R is the vector determining the action of external forces. In Eq. (1), the repeated indices imply summation, and the short notation for the derivatives is used $(\cdot)_{,t} = \partial(\cdot)/\partial t$, $(\cdot)_{,k} = \partial(\cdot)/\partial x_k$.

All quantities are dimensionless, nondimensionalization is performed using the following formulas (here, dimensional values are denoted by primes)

$$t = \frac{U_\infty t'}{d}, \ x = \frac{x'}{d}, \ p = \frac{p'}{\rho_\infty U_\infty^2}, \ u = \frac{u'}{U_\infty}, \ T = \frac{c_V T'}{U_\infty^2}, \ \rho = \frac{\rho'}{\rho_\infty},$$

For the Reynolds Re, Prandtl Pr, Mach M, and Strouhal St numbers the following expressions are used

$$Re = \frac{\rho_\infty U_\infty d}{\mu}, \ Pr = \frac{\mu c_p}{\kappa}, \ M = \frac{U_\infty}{c_\infty}, \ St = \frac{fd}{U_\infty}.$$

Here, d is the diameter of the cylinder; ρ_∞, p_∞, U_∞ are the free-stream density, pressure, and velocity; κ, μ are the thermal conduction and viscosity coefficients; c_V, c_p are the specific heats at constant volume and pressure; $c_\infty = \sqrt{\gamma p_\infty / \rho_\infty}$ is the free-stream sonic velocity; $\gamma = 1.4$ is the specific heat ratio; and f is a characteristic vortex shedding frequency. In the following text M = 0.1 and Pr = 0.72. With this choice, the present results are in good agreement with the results obtained for the case of an incompressible viscous fluid (see Section 2.3).

For the numerical solution of the problem, an unbounded physical domain is replaced by a finite region Σ by adding artificial boundaries (Fig. 1). Because the exact conditions for the variables at these boundaries are unknown, their position is chosen so that the distortion of the flow in the region of interest is small. In this paper, the input Γ_{in}, output Γ_{out}, and side Γ_{side} boundaries are located at $x_1 = -20$, $x_1 = 50$, and $x_2 = \pm 20$. Different positions of the end face planes Γ_{end}, $x_3 = \pm L/2$ are considered, which makes it possible to influence the structure of a three-dimensional flow (the choice of L is discussed further in Section 3.1).

2.1. Initial and Boundary Conditions

At the initial instant of time $t = 0$, it is assumed that in the entire field $u = 0$, $p = p_0 = 1/(\gamma M^2)$ and $T = T_0 = 1/[\gamma(\gamma - 1)M^2]$.

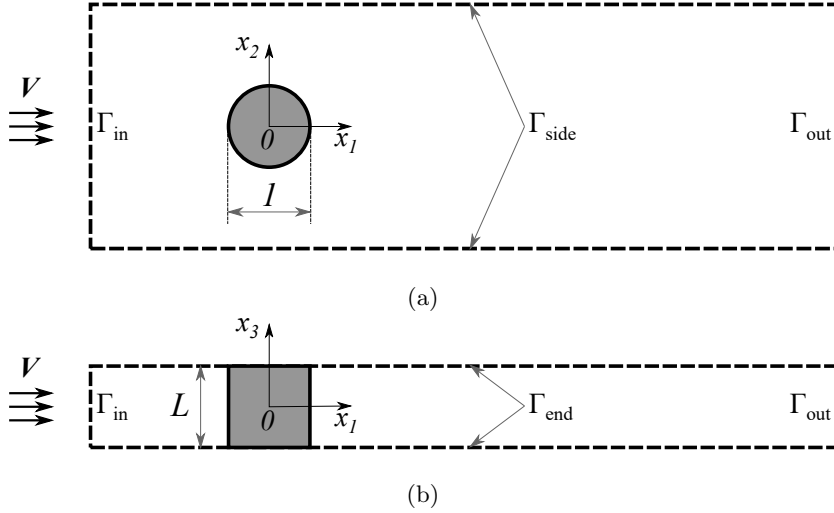Fig. 1: Schematic representation of the computational domain in planes x_1x_2 (a) and x_1x_3 (b).

At the inflow boundary Γ_{in}: $\boldsymbol{u} = \boldsymbol{V}(t)$, $p = p_0$, $T = T_0$. Here, $\boldsymbol{V}(t) = (V_1, V_2, V_3)^*$ determine the law of cylinder initial acceleration from rest to motion with constant velocity (in the inertial frame of reference associated with the resting flow). In the frame of reference associated with the cylinder the inertial forces must also be taken into account in (1): $\boldsymbol{F} = (V_{1,t}, V_{2,t}, V_{3,t})^*$. If $V_i(t) = \delta_{1i}$, then the problem is equivalent to the instantaneous onset of the motion of the cylinder in a fluid at rest. As a result, waves of pressure appear in the computational domain. Their reflection from the far boundaries slows down and distorts the process of reaching a periodic regime. Therefore, at the initial time interval $0 \leqslant t \leqslant t_*$, the velocity $V_1(t)$ is smoothly changed from $V_1(0) = 0$ to $V_1(t_*) = 1$, then $V_1(t) = 1$ for $t \geqslant t_*$. In addition, $V_2(t) \neq 0$ for $t \in (0, t_*)$ ($V_2(t) = 0$ for $t \geqslant t_*$) — this is a violation of the problem symmetry with respect to the plane $x_2 = 0$, which reduces the time of reaching the periodic regime. The third component $V_3(t) = 0$ for $t \geqslant 0$. In the presented calculations $t_* = 5$.

At the side and outflow boundaries $\Gamma_{\text{side}} \cup \Gamma_{\text{out}}$: $\partial u_i/\partial \boldsymbol{n} = 0$, $p = p_0$, $T = T_0$, $\boldsymbol{n}$ is a normal vector.

At the end face planes Γ_{end}: $\partial u_1/\partial \boldsymbol{n} = \partial u_2/\partial \boldsymbol{n} = 0$, $u_3 = 0$, $\partial T/\partial \boldsymbol{n} = 0$. These expressions are the conditions of symmetry (another interpretation is: the conditions for the absence of a flow of mass and heat across the planes Γ_{end} and the absence of tangential stresses).

On the cylinder surface, the velocity no-slip $\boldsymbol{u} = 0$ and adiabatic-wall (zero heat flux) conditions $\partial T/\partial \boldsymbol{n} = 0$ are prescribed.

2.2. Finite Element Formulation

Consider a partition of computational domain into tetrahedra elements (or triangles in the two-dimensional case), $\Sigma = \bigcup_{e=1}^{n_T} T_e$. Let $\mathcal{V}^h, \mathcal{W}^h$ be finite-dimensional spaces of continuous piecewise linear trial and weighing functions, respectively, constructed in the standard way for the finite element method. Then the stabilized finite element method GLS (Galerkin Least-Squares) for the equations (1) with boundary and initial conditions (Section 2.1) is formulated as follows: find $\boldsymbol{Y}^h \in \mathcal{V}^h$ such that for any $\boldsymbol{W}^h \in \mathcal{W}^h$

$$\int_\Sigma \boldsymbol{W}^h \cdot (\boldsymbol{A}_0^h \boldsymbol{Y}_{,t}^h + \widetilde{\boldsymbol{A}}_i^h \boldsymbol{Y}_{,i}^h - \boldsymbol{R}^h) + \boldsymbol{W}_{,i}^h \cdot (\boldsymbol{K}_{ij}^h \boldsymbol{Y}_{,j}^h)d\Sigma$$

$$- \int_{\partial\Sigma} \boldsymbol{W}^h \cdot (\boldsymbol{K}_{ij}^h \boldsymbol{Y}_{,j}^h n_i)d\Gamma$$

$$+ \sum_{e=1}^{n_T} \int_{T_e} (\boldsymbol{L}^* \boldsymbol{W}^h) \cdot \tau_s (\boldsymbol{L}\boldsymbol{Y}^h - \boldsymbol{R}^h)d\Sigma = 0,$$

here, the matrix τ_s defines stability properties of the method; $\boldsymbol{L} = \boldsymbol{A}_0^h \partial/\partial t + \widetilde{\boldsymbol{A}}_i^h \partial/\partial x_i - \partial/\partial x_i(\boldsymbol{K}_{ij}^h \partial/\partial x_j)$ is a differential operator; $\widetilde{\boldsymbol{A}}_i^h \boldsymbol{Y}_{,i}^h = \boldsymbol{A}_i^h \boldsymbol{Y}_{,i}^h + \boldsymbol{P}_{,i}^h$; the superscript symbol 'h' denotes that the values are calculated based on an approximate solution. The additional term (the latter) is introduced in the standard Galerkin variational equation to improve the stability of the numerical method (see, for instance the review [14]). Implicit Euler method for the time-derivative is applied. The original problem is reduced to a system of nonlinear algebraic equations, which is solved by Newtons iterative method with the generalized minimum-residual algorithm (GMRES). More details on the use of the present numerical approach can be found in [15–18].

2.3. Influence of the Numerical Parameters

To justify the sizes of the computational domain and the steps of the computational grid, we consider the results obtained on 6 two-dimensional grids (Table 1). Three nested subregions with different grid steps (transitions between subregions are smooth) are distinguished in the computational domain: the far wake ($x_1 > -5$, $|x_2| < 7.5$) with step

3

h_w, the near wake ($-1.5 < x_1 < 11$, $|x_2| < 2$) with step h_{nw} and a subregion near the surface of the body with step h_b. Outside the far wake region, the step is h_g. The grids A_{2D}^1, A_{2D}^2, A_{2D}^3 are distinguished by the space step; A_{2D}^4, A_{2D}^4, A_{2D}^6 are distinguished by the sizes of the domain.

The following characteristics were selected as criteria for determining the degree of influence of the distance from the cylinder to the far borders and grid steps: mean and root-mean-square values of the drag coefficient $\overline{C_D}, \delta C_D$, root-mean-square value of the lift coefficient δC_L, Strouhal number St, and flow patterns in a rectangular region $-1 \leqslant x_1 \leqslant 6$, $-2 \leqslant x_2 \leqslant 2$.

Table 1 shows the results of calculating the forces and the Strouhal number for $Re = 300$. The data obtained on the grid A_{2D}^2, differ by less than 5% (except for δC_D on the coarse grid A_{2D}^1 — the difference here is 5.6%) from the results on the grids A_{2D}^1, A_{2D}^3, A_{2D}^4, A_{2D}^5, A_{2D}^6. The differences in $\overline{C_D}$ and St with values from [2, 19] are about 1% ($\overline{C_D} = 1.3769$, St = 0.2113, relationship St(Re) from [2] is explicitly given in [20]). Decrease in time step by a factor of two (from $\Delta t = 0.005$ to $\Delta t = 0.0025$) changes $\overline{C_D}$ and St by less than 0.3% and δC_L by less than 1%. A comparison of the pressure fields p for grids A_{2D}^1, A_{2D}^2 and A_{2D}^3 (Fig. 2 a-b) also shows the possibility of using a grid A_{2D}^2 for a qualitative study of the flow in the near-wake region of interest.

Further we use three-dimensional grids similar to the A_{2D}^2 in the sections $x_3 = $ const, i.e. $h_b = 0.01$, $h_{nw} = 0.05$, $h_w = 0.15$, $h_g = 0.3$ and time step $\Delta t = 0.005$. A comparison of the results of calculating the two-dimensional flow regime for $Re = 200$ in two- and three-dimensional (for $L = 3$) formulations is given in Fig. 2c, the difference between $\overline{C_D}, \delta C_D, \delta C_L$, St is less than 0.5%.

Based on these results and the consistency of the further results with the data of other authors (see the next two sections) we believe that the accuracy should be sufficient for a qualitative description of the mechanisms of transition to three-dimensionality.

3. Identification of Growth and Decay Regions and Responsible Mechanisms

This section describes the flow regimes under consideration and the approach on the basis of which the mechanisms and regions determining the growth and decay of small three-dimensional perturbations of a two-dimensional periodic base flow are singled out. In the next section (Section 4), this approach is used to analyze the process of transition to three-dimensionality for modes A and B. In these sections we describe the flow in terms of velocity $\boldsymbol{u}$ and vorticity $\boldsymbol{\omega} = \nabla \times \boldsymbol{u}$ assuming that the flow is incompressible (in calculations M = 0.1 therefore compressibility effects are insignificant).

3.1. The considered flow regimes
For a fixed Reynolds number, the wavelengths λ of linearly unstable perturbations for modes A and B belong to

the intervals $0 < \lambda_A^{min} < \lambda < \lambda_A^{max}$ and $0 < \lambda_B^{min} < \lambda < \lambda_B^{max}$, see [2]. The symmetry conditions at the end faces of the computational domain (Section 2.1) impose restrictions on the set of admissible linearly unstable perturbations: $\lambda = 2L/n$, $n = 1, 2, ...$ By decreasing the distance L between the end planes confining the flow, the set of linearly unstable perturbations can be reduced (up to an empty set). Taking this into account, the length of the cylinder L is chosen so that the constraints are satisfied by a single value λ, which is close to the critical (the most unstable) values $\lambda_A \approx 4$ and $\lambda_B \approx 0.8$ [2]. Further in the article we will consider the following two flow regimes (Fig. 3).

- Mode A for $Re = 220$ and $L = 2.0$.
- Mode B for $Re = 300$ and $L = 0.4$.

For these cases the behavior of half of the perturbations wavelength along the x_3 axis is modeled in the computational domain. In a real flow for $Re = 300$ mode B develops together with mode A, but due to the specified length of the computational domain along the x_3 axis the unstable perturbations of mode A are eliminated and the 'pure' mode B can be modeled.

In Fig. 3 for the two modes A and B under consideration, the graphs of $C_L(t)$ and the isosurface $u_3 = \pm$const and $\omega_3 = \pm$const are given. The flow fields are given for two instants of time corresponding to the initial and late stages of the development of the three-dimensional instability. At relatively short times for mode A we observe a distinct symmetry with respect to the plane $x_3 = 0$ (Fig. 3d). For the developed flow the three-dimensional pattern is different and more complicated along the x_3 axis (Fig. 3h). For mode B, the flow structure is similar for large and small t (Fig. 3 e, f, i, j). In this case, the nonlinear stage of perturbation development does not violate their symmetry along the x_3 axis and slightly distorts their spatial structure in comparison with the linear stage. We are interested in the causes of the emergence of modes A and B, so we will consider the development of a three-dimensional flow at times close to $t = 70$ for mode A and to $t = 38$ for mode B (Fig. 3 a, b). At these times the flow differs from the two-dimensional flow sufficiently, so that small three-dimensional perturbations are distinguishable from computational errors.

We will assume that the causes of the appearance of modes A and B are flow properties in the region of formation of vortices in the near wake, and the development of three-dimensionality downstream is a consequence of the instability of the flow arising near the cylinder. This is confirmed by the results [13], which show that for modes A and B, the periodic flow in the developed vortex wake is stable with respect to linear three-dimensional perturbations. Therefore, in what follows we restrict ourselves to a consideration of the region near the cylinder ($0.5 < x_1 < 3$).

3.2. Extraction of Linear Perturbations
When the three-dimensional perturbations are small (at the initial stages of the development of the flow with re-

	$W_{in} \times W_{out} \times H$	h_b	h_{nw}	h_w	h_g	$\overline{C_D}$	δC_D	δC_L	St
A_{2D}^1	$20 \times 50 \times 20$	0.02	0.1	0.3	0.6	1.3366	0.0506	0.5965	0.2080
A_{2D}^2	$20 \times 50 \times 20$	0.01	0.05	0.15	0.3	1.3564	0.0536	0.6234	0.2089
A_{2D}^3	$20 \times 50 \times 20$	0.005	0.025	0.075	0.15	1.3659	0.0558	0.6361	0.2094
A_{2D}^4	$20 \times 100 \times 20$	0.01	0.05	0.15	0.3	1.3615	0.0544	0.6289	0.2094
A_{2D}^5	$40 \times 50 \times 20$	0.01	0.05	0.15	0.3	1.3513	0.0536	0.6218	0.2087
A_{2D}^6	$20 \times 50 \times 40$	0.01	0.05	0.15	0.3	1.3616	0.0550	0.6310	0.2093

Table 1: Parameters of two-dimensional computational grids and their effect on the calculation results for Re = 300. W_{in}, W_{out} and H are the distances from the center of the cylinder to the inlet (Γ_{in}), outlet (Γ_{out}), and side (Γ_{side}) boundaries of the computational domain.

(a) Re = 300, grids A_{2D}^2 and A_{2D}^1.   (b) Re = 300, grids A_{2D}^2 and A_{2D}^3.   (c) Re = 200, 2D and 3D calculations.
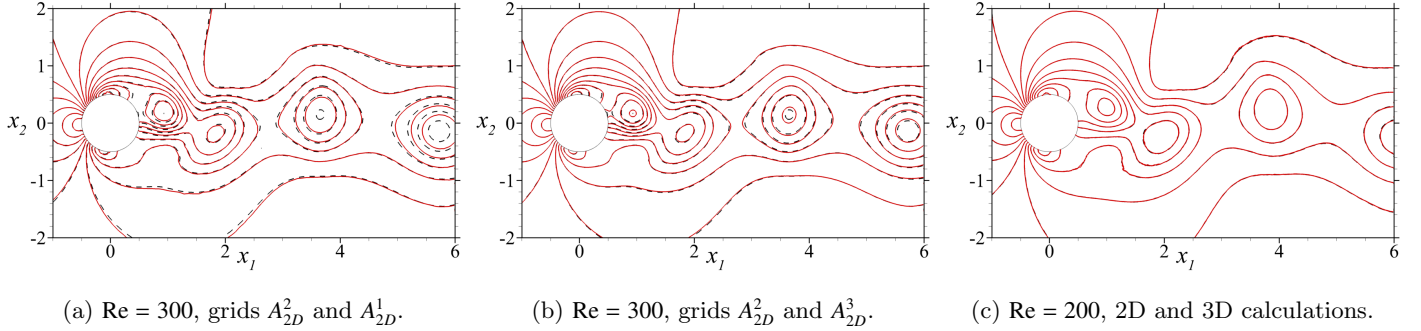
Fig. 2: Influence of the computational grid on the pressure field p in the near wake. Dashed lines are calculations on a two-dimensional grid A_{2D}^2; solid lines are calculations on two-dimensional grids A_{2D}^1 (a), A_{2D}^3 (b) and on a three-dimensional grid with $L = 3$ (c). The pressure isolines correspond to the values $p = 70.5, 70.6, \ldots, 71.9$. For the three-dimensional case, the lines in the section $x_3 = 0$ are shown. The time corresponds to the maximum value of the lift coefficient.

spect to time), by virtue of the symmetry conditions on the end planes, approximate expressions for velocity and vorticity fields can be used:

$$
\begin{aligned}
&\boldsymbol{u}(x_1, x_2, x_3, t) = \boldsymbol{U}(x_1, x_2, t) + \boldsymbol{u}'(x_1, x_2, x_3, t), \\
&\boldsymbol{\omega}(x_1, x_2, x_3, t) = \boldsymbol{\Omega}(x_1, x_2, t) + \boldsymbol{\omega}'(x_1, x_2, x_3, t), \\
&\boldsymbol{u}' = (v_1, v_2, 0)^* \sin \gamma x_3 + (0, 0, v_3)^* \cos \gamma x_3, \\
&\boldsymbol{\omega}' = (\zeta_1, \zeta_2, 0)^* \cos \gamma x_3 + (0, 0, \zeta_3)^* \sin \gamma x_3,
\end{aligned}
\tag{2}
$$

here, $\boldsymbol{U}(x_1, x_2, t) = (U_1, U_2, 0)^*$ and $\boldsymbol{\Omega}(x_1, x_2, t) = (0, 0, \Omega)^*$ are velocity and vorticity of the base flow; $\boldsymbol{u}'$ and $\boldsymbol{\omega}'$ are small perturbations; $v_i = v_i(x_1, x_2, t)$ and $\zeta_i = \zeta_i(x_1, x_2, t)$, $i = 1, 2, 3$; $\gamma = \pi/L$. The functions v_i and ζ_i can be found using the Fourier series expansion of the calculated solution of the three-dimensional problem. The possibility of using relations (2) for the regimes and stages of development of the flow considered in this work was verified by comparison of the total and truncated perturbation fields.

The fields of small three-dimensional perturbations of modes A and B can also be found in two steps: the search for the base flow solution (the solution of the problem in a two-dimensional formulation) and the solution of the spectral problem arising after the linearization of the three-dimensional Navier-Stokes equations for perturbations. In this manner, perturbation fields were found numerically in the process of applying the Floquet theory in the paper [2]. Our results for early stages of instability development (Fig. 3 c-f) are consistent with the structure of linear three-dimensional perturbations obtained in [2].

3.3. Identification of Regions and Mechanisms

Further we derive the system of equations for small perturbations in terms of velocity and vorticity. The linearization of the vorticity transport equation with respect to the perturbations leads to the relation

$$
\frac{D\boldsymbol{\omega}'}{Dt} = -(\boldsymbol{u}' \cdot \nabla)\boldsymbol{\Omega} + (\boldsymbol{\omega}' \cdot \nabla)\boldsymbol{U} + (\boldsymbol{\Omega} \cdot \nabla)\boldsymbol{u}' + \frac{1}{\text{Re}}\nabla^2\boldsymbol{\omega}', \quad (3)
$$

here, $D/Dt = \partial/\partial t + \boldsymbol{u} \cdot \nabla \approx \partial/\partial t + \boldsymbol{U} \cdot \nabla$ is the substantial derivative. Using Eq. (2) and excluding v_3, ζ_3 from the equations we obtain a closed system on $\boldsymbol{\zeta}(x_1, x_2, t) = (\zeta_1, \zeta_2)^*$ and $\boldsymbol{v}(x_1, x_2, t) = (v_1, v_2)^*$:

$$
\frac{D\boldsymbol{\zeta}}{Dt} = \gamma\Omega\boldsymbol{v} + (\boldsymbol{\zeta} \cdot \nabla)\boldsymbol{U} + \frac{1}{\text{Re}}\left(\nabla^2\boldsymbol{\zeta} - \gamma^2\boldsymbol{\zeta}\right), \tag{4}
$$

$$
\gamma\boldsymbol{\zeta} = (\nabla \cdot \boldsymbol{v}_{,2} - \gamma^2 v_2, \gamma^2 v_1 - \nabla \cdot \boldsymbol{v}_{,1})^*. \tag{5}
$$

All functions in these equations depend only on x_1, x_2, t and vectors are assumed to be two-dimensional. The perturbation components along the x_3 axis can be found from the relations $\gamma v_3 = v_{1,1} + v_{2,2}$ and $\gamma\zeta_3 = -\zeta_{1,1} - \zeta_{2,2}$.

One can rewrite Eq. (4) in a more convenient form for analysis. For this we denote the positive eigenvalue of the strain rate tensor as S and Φ is the angle between the principal direction and the x_1 axis. We write the vectors $\boldsymbol{v}$, $\boldsymbol{\zeta}$ in terms of the polar representation, i.e.

$$
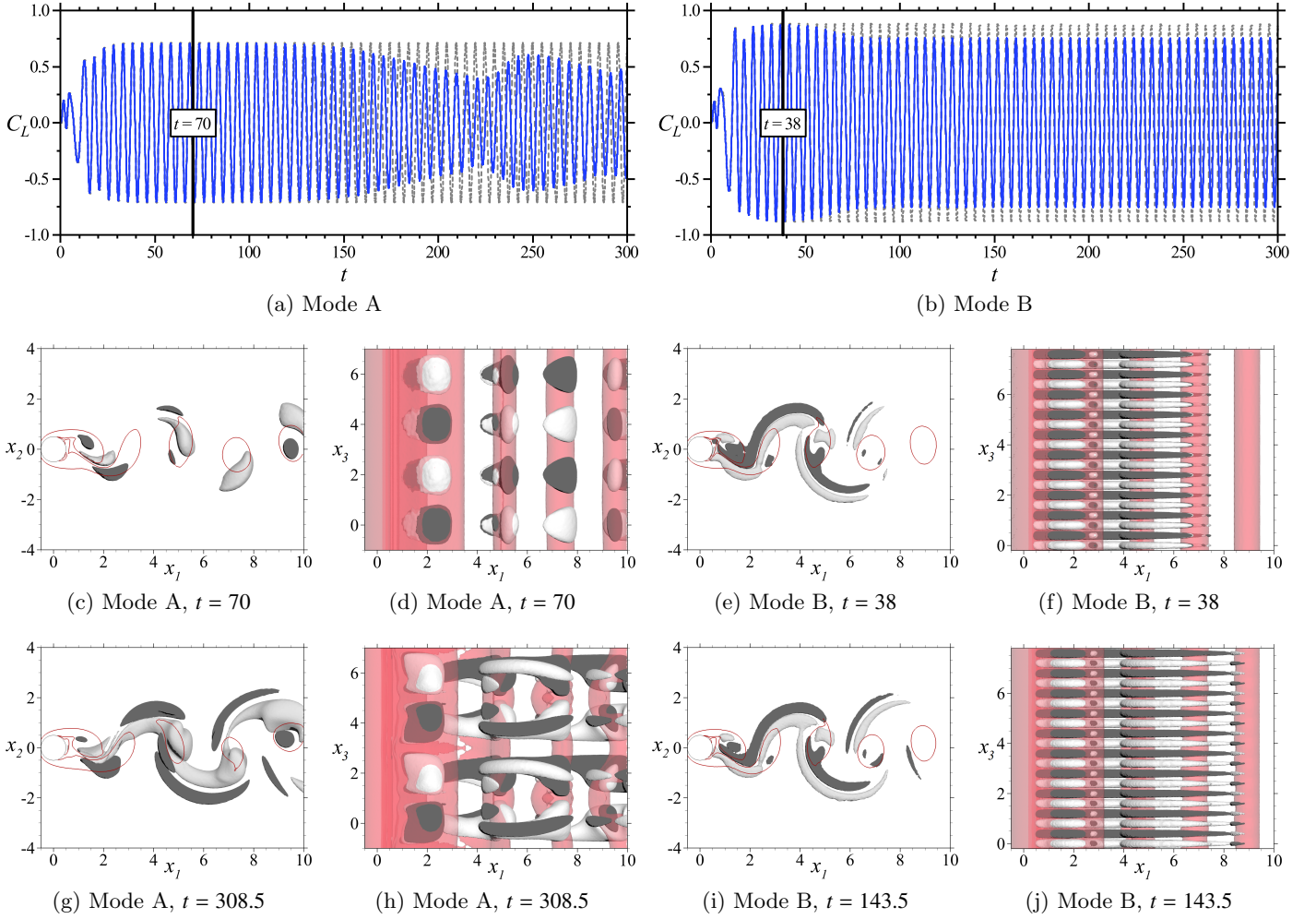\boldsymbol{\zeta} = \zeta(\cos\theta, \sin\theta)^*, \quad \boldsymbol{v} = v(\cos\theta_1, \sin\theta_1)^*. \tag{6}
$$

5

(a) Mode A   (b) Mode B

(c) Mode A, $t = 70$ (d) Mode A, $t = 70$ (e) Mode B, $t = 38$ (f) Mode B, $t = 38$

(g) Mode A, $t = 308.5$ (h) Mode A, $t = 308.5$ (i) Mode B, $t = 143.5$ (j) Mode B, $t = 143.5$

Fig. 3: The flow regimes considered in the present paper: on the left — mode A for $\mathrm{Re} = 220$, $L = 2$; on the right — mode B for $\mathrm{Re} = 300$, $L = 0.4$. (a), (b) — the dependence of the lift coefficient on time for a three-dimensional (solid lines) and two-dimensional flow (dashed lines). The initial (c-f) and late (g-j) stages of three-dimensional flow development are shown. Depicted isolines and isosurfaces correspond to constant values of u_3 (black and gray colors) and ω_3 (red color): $u_3 = \pm 0.008$ (c-d), $u_3 = \pm 0.002$ (e-f), $u_3 = \pm 0.1$ (g-h), $u_3 = \pm 0.02$ (i-j); $\omega_3 = \pm 1$ (c-j). The data in the $x_1 x_3$-plane (d, f, h, j) are duplicated along x_3-axis, in fact, the calculated domain is $|x_3| \leqslant L/2$.

(a) Scheme for notations   (b) Action of $\mathcal{S}_\zeta$, $\mathcal{S}_\theta$ (c) Action of $\mathcal{V}_\zeta$, $\mathcal{V}_\theta$
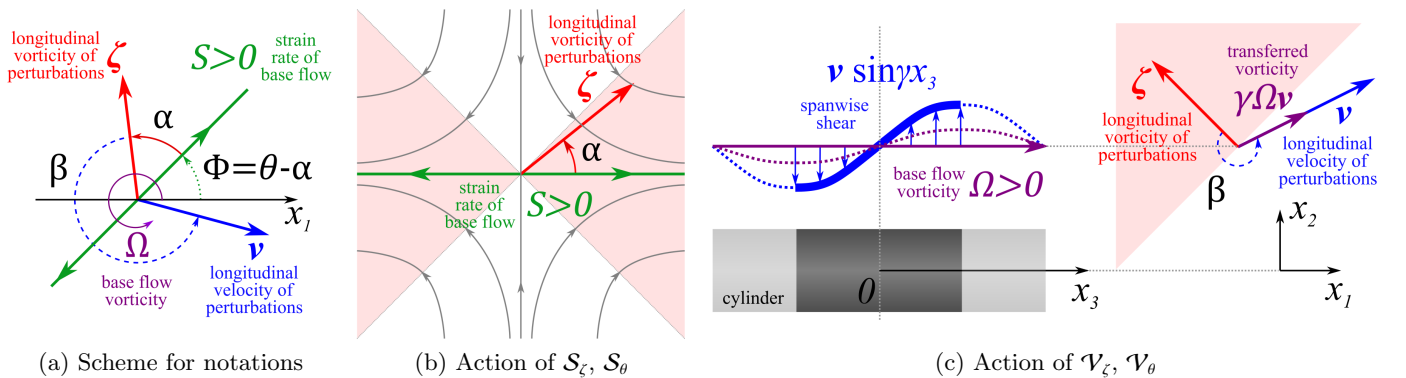
Fig. 4: A schematic description of the action of physical mechanisms in Eqs. (7) and (8). In the present work the terms 'longitudinal' and 'streamwise' mean the projection of vectors onto the plane $x_1 x_2$.

It is convenient to introduce additional angles: angle α between the principal axis and $\boldsymbol{\zeta}$, $\alpha = \theta - \Phi$ and angle β between vectors $\boldsymbol{\zeta}$ and $\boldsymbol{v}$, $\beta = \theta_1 - \theta$ (Fig. 4). After

transformations Eq. (4) takes the form

$$\frac{D \ln \zeta}{Dt} = \underbrace{S \cos 2\alpha}_{\mathcal{S}_\zeta} + \underbrace{\frac{\gamma \Omega v}{\zeta} \cos \beta}_{\mathcal{V}_\zeta} + \underbrace{\frac{1}{\zeta^2 \mathrm{Re}} \left(\boldsymbol{\zeta} \cdot \nabla^2 \boldsymbol{\zeta} - \gamma^2 \zeta^2 \right)}_{\mathcal{D}_\zeta}, \quad (7)$$

$$\frac{D\theta}{Dt} = \underbrace{-S\sin 2\alpha}_{\mathcal{S}_\theta} + \underbrace{\frac{\gamma\Omega\nu}{\zeta}\sin\beta}_{\mathcal{V}_\theta} + \underbrace{\frac{1}{\zeta^2\mathrm{Re}}\left(\zeta\times\nabla^2\zeta\right)\cdot e_3}_{\mathcal{D}_\theta} + \underbrace{\frac{1}{2}\Omega}_{\mathcal{R}_\theta}\ .$$

(8)

Here, e_3 is the unit vector along the x_3-axis. There is a linearized substantial derivative on the left-hand side in Eqs. (7) and (8). This form of equations for the perturbations allows us to consider the quantities ζ and θ in the Lagrangian description as characteristics associated with a particular fluid particle of the base flow. The rate of amplitude or angle change in a fluid particle can be described with 3 or 4 terms, having a clear connection with the basic physical mechanisms that determine the development of vorticity in the flow. Each term on the right-hand side of Eq. (7) tends to increase the amplitude ζ of the perturbations when it is positive and the more it is, the more intense the growth is. If the term is negative, then it tends to reduce ζ. Let us consider the action of each term separately.

The first term $(\mathcal{S}_\zeta, \mathcal{S}_\theta)$ describes the mechanism of vorticity change due to the action of strain rate tensor field of the base flow. The amplitude ζ tends to grow if the angle between the vorticity vector ζ and the principal axis (S) is less than $\pi/4$ (filled regions in Fig. 4b) and θ is changed to reduce the angle between the principal axis and vector ζ.

The second term $(\mathcal{V}_\zeta, \mathcal{V}_\theta)$ is related to shear deformation of the base flow vortex lines. A spanwise shear deforms the vortex lines of the base flow and causes generation of streamwise vorticity as is schematically shown in Fig. 4c. Thus, $\gamma\Omega\nu\Delta t$ is vorticity of the base flow transferred to the plane $x_3 = 0$ under the influence of shear $\nu\sin\gamma x_3 \neq 0$ during the time interval Δt. The amplitude ζ tends to grow if the transferred vorticity has positive projection on the vorticity vector ζ (filled region in Fig. 4c). The angle θ is increased or decreased according to the direction of the transferred vorticity of the basic flow to the spanwise plane (more precisely, according to the sign of $\Omega\sin\beta$).

The third term $(\mathcal{D}_\zeta, \mathcal{D}_\theta)$ describes the action of viscous diffusion, which stabilizes perturbations, as will be seen below.

The fourth term $(\mathcal{R}_\theta)$ is the rotation of a fluid particle as a rigid body. It changes only the direction of the vorticity vector.

Having numerical solutions in a three-dimensional formulation, we can find all necessary values on the right-hand side, and we can assess to what extent and in what regions each physical mechanism has a stabilizing or destabilizing effect on the flow. In this paper we consider fields for mechanisms of amplitude change, Eq. (7), however, the same analysis can be applied to the equation for angle, Eq. (8).

The behavior of the terms in Eq. (7) can be estimated in two limiting cases $\gamma \to 0$ and $\gamma \to \infty$. Parameter γ does not influence the first term $(\mathcal{S}_\zeta)$. The second term $(\mathcal{V}_\zeta)$

vanishes as $\gamma \to 0$ and approaches $\Omega\cos\beta$ as $\gamma \to \infty$ (to estimate the order of ν/ζ, Eq. (5) is used). The third term has two limits $\zeta\cdot\nabla^2\zeta/(\zeta^2\mathrm{Re})$ and $-\gamma^2/\mathrm{Re}$ as $\gamma \to 0$ and $\gamma \to \infty$. These estimates give a rough idea of the influence of the wavelength of perturbations on various terms in Eq. (7). However, it does not give unambiguous conclusions about the influence of the mechanisms at the wavelengths close to the critical one. A more detailed study of the effect of γ is needed, which is beyond the scope of the present paper.

Consider the idealized situation, when in the entire flow Ω, S and Φ are constants, the choice of the coordinate system allows us to consider $\Phi = 0$. This flow is an exact solution of the Navier-Stokes equations [21]. If $|\Omega|/2 > S$, then rotation prevails and the streamlines are similar ellipses; if $|\Omega|/2 < S$, then the stretching rate prevails and the streamlines are hyperbolas; the equality $|\Omega|/2 = S$ corresponds to the Couette flow. The three-dimensional instability of two-dimensional flows of this type was investigated in [11, 22–24]. These results can be used to estimate the wavelengths of developing three-dimensional perturbations for a two-dimensional flow with localized vorticity [25]. Application of these theoretical results to the instability of a flow around a cylinder is discussed in [4, 6]. It was shown that mode A instability resembles elliptic instability judging by spatial structures and estimations of wavelengths and growth rates. Also, it was suggested that mode B is caused by hyperbolic instability of the braid shear layer.

In a general case, the influence of the base flow on the behavior of perturbations in a fluid particle is determined by three fields Ω, S, Φ depending on the coordinates, see Eqs. (7) and (8). The relation between Ω and S at each point determines the type of instantaneous local flow in the neighborhood of this point. For an incompressible fluid, these regions can be distinguished by considering the sign of the invariant

$$Q = -\frac{1}{2}\mathrm{trace}(\nabla U)^2 = \frac{1}{4}\Omega^2 - S^2, \quad (\nabla U)_{ij} = U_{i,j}. \quad (9)$$

For $Q > 0$ (the rotation prevails) the singular points are center-type. For $Q < 0$ (the stretching prevails) the singular points are saddle-type. The regions with $Q > 0$ and $Q < 0$ are called elliptic and hyperbolic flow regions respectively. The locations of these regions and the domains in which the perturbations are concentrated are shown in Fig. 5 for modes A and B.

4. Comparative Analysis of Mechanisms

On the basis of the data on the direction of the vectors ζ and their amplitude a scheme of the development of perturbations ζ is constructed in Fig. 6. The arrows schematically determine the positions of the local perturbation regions and the direction of the vectors ζ. To estimate the growth rate we also consider the variation in time of the maximum value ζ_{max} of ζ in the local perturbed region, Fig. 7. The influence of each mechanism is distinguished
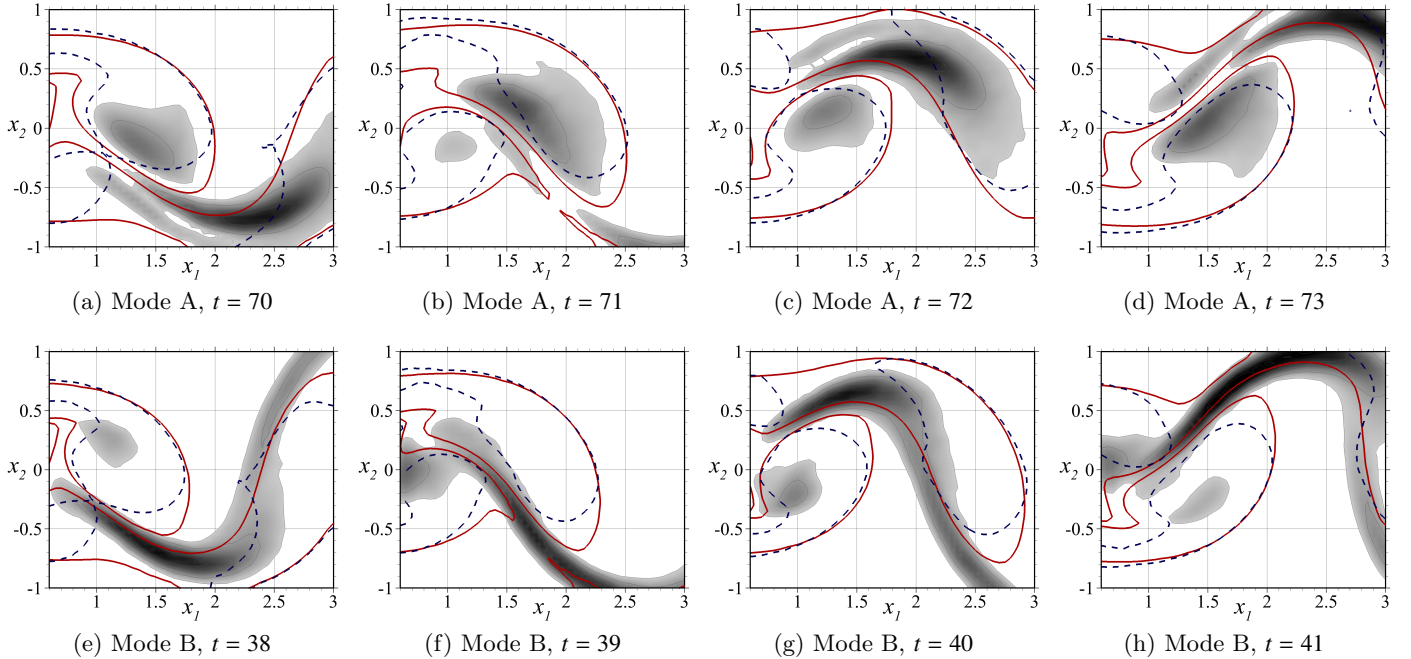
Fig. 5: Evolution of perturbed flow regions for modes A (a-d) and B (e-h). Filled gray zones are the ζ field for $\zeta \gtrsim 0.2 \max \zeta$ (the larger ζ, the darker the color), solid lines are the lines of $|\Omega| = \text{const}$ (base flow), dashed lines are the lines of $Q = 0$ (base flow).

in Figs. 8 and 9, they show the variation of $D(\zeta^2/2)/Dt$, and the contribution of each mechanism on the right-hand side of Eq. (7) to growth and decay of perturbations for two moments in time $t = 71, 72$ for mode A and $t = 39, 40$ for mode B (it corresponds to the second and the third rows on scheme in Fig. 6). Below we discuss stages of the development of perturbations for modes A and B with respect to these data.

4.1. The Evolution of the Perturbed Regions: mode A

4.1.1. Stage I: Perturbations originate and grow in a forming vortex

In Fig. 5b one can see that a new perturbed region appears ($x_1 \approx 1$, $x_2 \approx -0.2$) in the bottom vortex in the beginning of its formation (the time corresponds to the second row of the scheme in Fig. 6a, see arrow 1_2). The region is growing in the elliptic part of the flow until the forming vortex begins to separate from the cylinder (Fig. 5d for the bottom vortex and arrow 1_4 in Fig. 6a).

The origin of perturbations in a new vortex happens mostly because of term $\mathcal{V}_\zeta$ (see mechanisms fields at $t = 71$, Fig. 8a, c). That is why the appearance of new perturbations in a forming vortex (Fig. 5b) is connected with the shear deformation of the main vortex, and apparently can be induced by the perturbed region in the previous (downstream) vortex, as described in [4]. Subsequent growth of three-dimensional structures is mostly related to the vortex line stretching, $\mathcal{S}_\zeta$ (Fig. 8b, f). However, shear deformations of the vortex lines of the base flow $\mathcal{V}_\zeta$ make a significant contribution, both destabilizing and stabilizing (Fig. 8c, g). This contribution of the mechanism $\mathcal{V}_\zeta$ is an indirect confirmation of the well-known property of mode

A — the emergence of a distinct wave-like curvature of the spanwise vortices (Fig. 3h). The viscous diffusion $\mathcal{D}_\zeta$ suppresses perturbations (Fig. 8d, h).

Perturbations grow at both stage I and II (Fig. 7a). One can see a slight change in the growth rate at $(t - t_0)/\tau \approx 0.4$ (point 1_4 in Fig. 7a). This change takes place when the perturbations are leaving the elliptic region and the second stage begins.

4.1.2. Stage II: Perturbations move outside the main vortex and intensively grow in the region of high deformation rates

The formed longitudinal vorticity is stretching in the braid region, where the main vortex is separated from the cylinder (arrow 2_2 in Fig. 6a). It approaches a new forming vortex upstream and induces the origin of a new region of perturbations (arrow 1_2). This new region goes through all these stages again. Based on the experimental results, a self-sustained process for mode A, where perturbations of the downstream vortex generate perturbation in the upstream vortex by Biot-Savart induction, was discussed in [4]. The head of the vortex loop (emerged from the downstream main vortex) is transferred upstream (relative to the main vortex) by the reversed flow, and then modifies the flow in the next forming vortex. This process establishes the spatial structure of mode A. Numerical results for the evolution of the disturbed region of mode A (Fig. 8) have clear correlation with this physical interpretation. The vortex loop development in our formulation corresponds to the evolution of ζ at stage II (in the hyperbolic region).

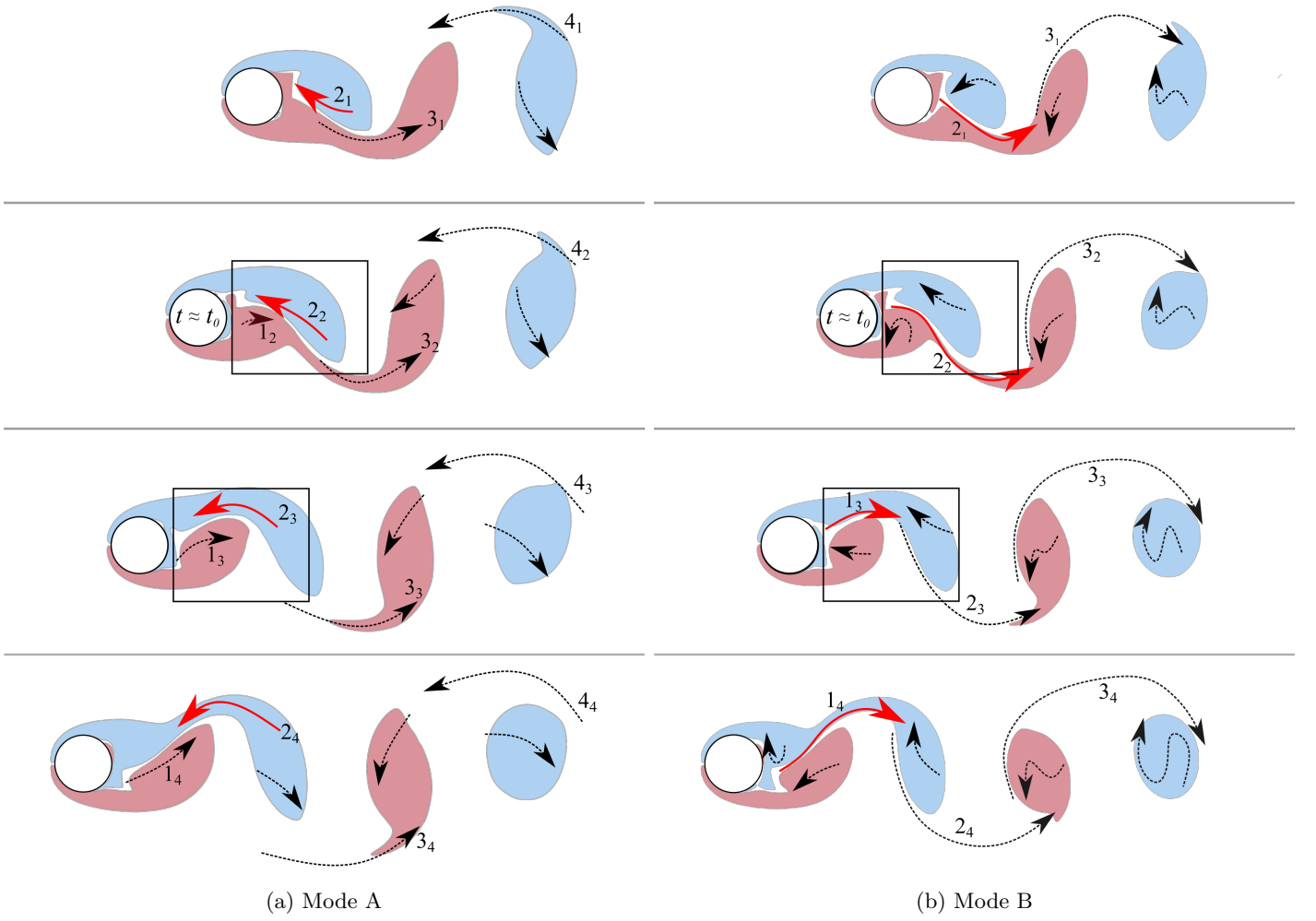The two stages of perturbations growth were discussed

8

(a) Mode A

(b) Mode B

Fig. 6: Schematic representation of the perturbations evolution for modes A (a) and B (b): vortices of the base flow and perturbed regions. The arrows show the regions where perturbations are concentrated and the orientation of vectors $\boldsymbol{\zeta}$. Numbers with subscripts correspond to the points in Fig. 7 (a number indicates the relative position of the region, a subscript indicates the row, i.e. a moment in time). In the second and third row, selected rectangular regions correspond to ones shown in Figs. 8 and 9.

(a) Mode A

(b) Mode B
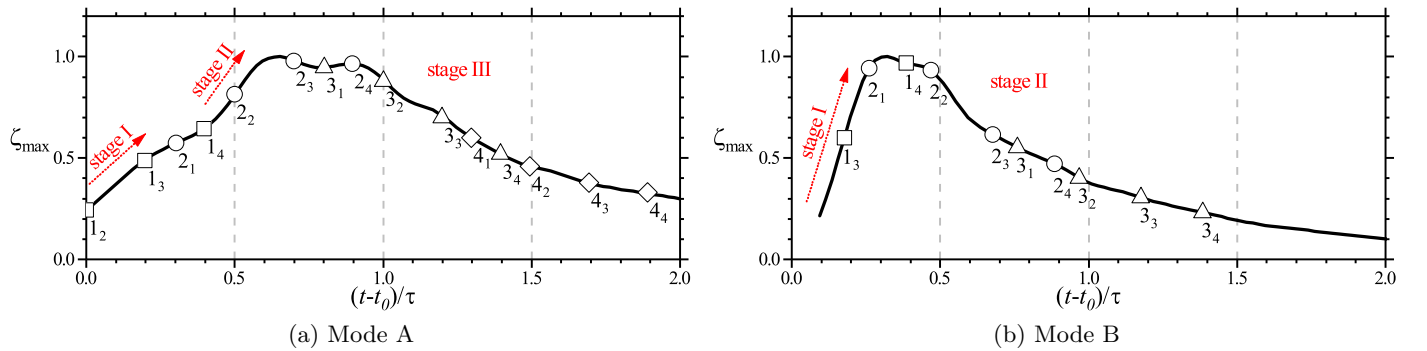
Fig. 7: Change of local maximum of ζ in the perturbed region of the flow for modes A (a) and B (b). Marked points correspond to the perturbed regions shown in Fig. 6. Value t_0 corresponds to the local extrema of lift coefficient C_L and τ is the vortex shedding period. Dotted lines show the estimates of the growth rates.

earlier in [7]. However, the second stage has been perceived as being of secondary importance and the elliptic instability (I stage) was considered as the main reason for the appearance of mode A. Our qualitative data for $\zeta(t)$

change in Fig. 7a show that at stage II the growth rate of linear perturbations is slightly greater. That is why it is not obvious which mechanisms trigger the transition to three-dimensionality when the Reynolds number exceeds
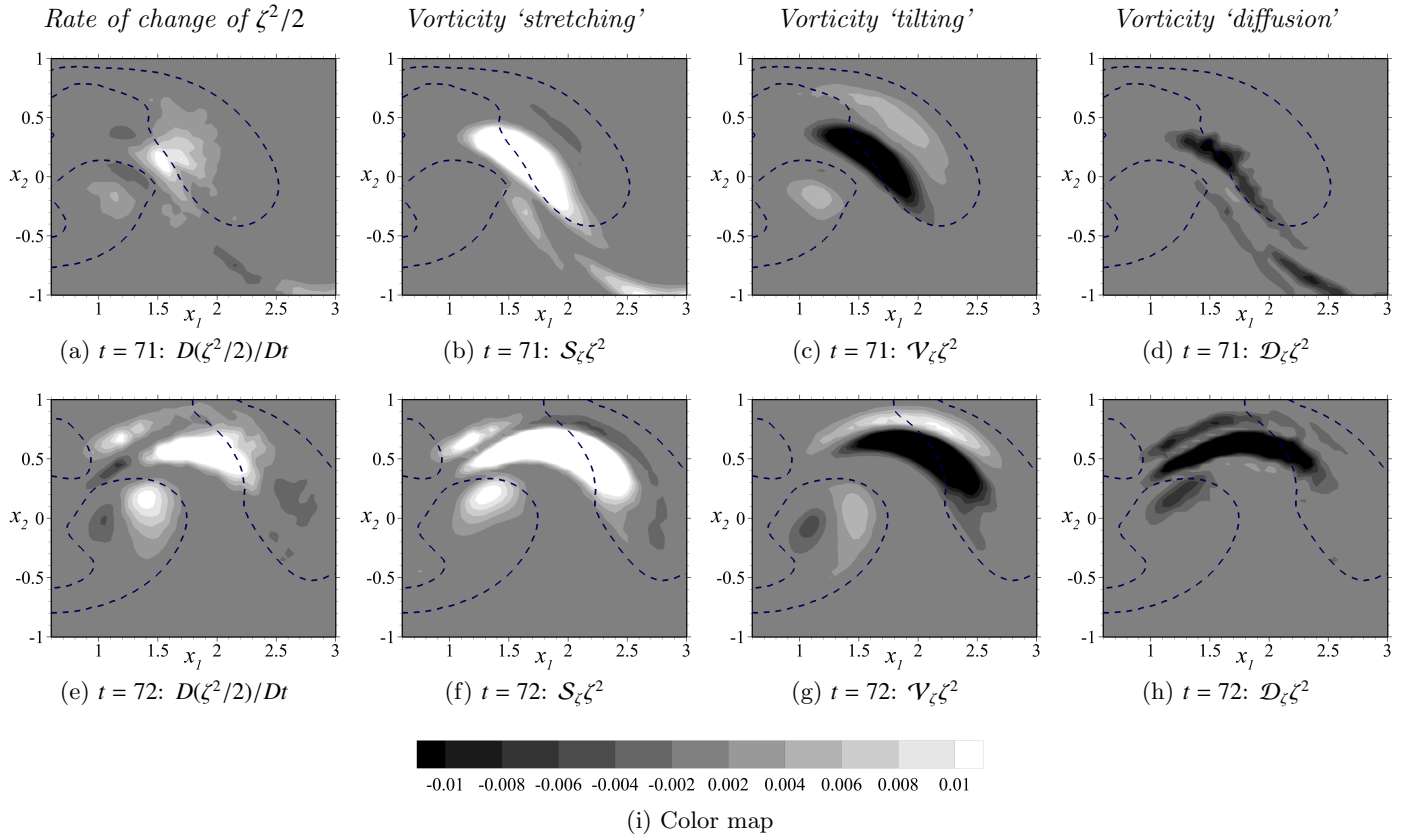
9

Fig. 8: The rate of variation of perturbation amplitude (multiplied by factor ζ) $D\zeta/Dt$ (a, e) in the fluid particle for mode A and the contribution of three mechanisms (multiplied by factor ζ^2): vorticity 'stretching' $\mathcal{S}_\zeta$ (b, f), 'tilting' $\mathcal{V}_\zeta$ (c, g), 'diffusion' $\mathcal{D}_\zeta$ (d, h). Dashed lines are the lines of $Q = 0$. The time corresponds to the second ($t = 71$) and third ($t = 72$) rows on the scheme in Fig. 6a. Limit values on the color map (i) are not the maximum and minimum of functions: function values greater than the upper limit (or less than the lower limit) are filled with one color corresponding to this limit.

the critical value: the instability of the flow in the elliptic region or in the hyperbolic region, or the reason for the transition is more complex and this instability cannot be explained considering only one of these simplified types of flow. We believe that it is necessary to take into account the second stage of perturbations development to estimate the critical Reynolds number by constructing models based on simplified flows. The necessity of consideration of stage II is implicitly confirmed by the work [13]. It was shown that the region of high deformation rates in the wake cannot be excluded from the subregion of local Floquet stability analysis to obtain the same dependence of Floquet multipliers on wavenumber as for the whole region of the flow.

4.1.3. Stage III: Perturbations are fading out

The considered region is decaying in the developed vortex street (Fig. 7a, stage III). However, it should be noted, that one can see two moments in time when new perturbations emerge (Fig. 6a) — upstream (arrow 1_2, discussed above) and downstream (arrow without a number inside the second vortex in the fourth row) from the considered perturbation region. The longitudinal vorticity formed downstream inside the elliptic region is growing while the

considered perturbations are decaying downstream. From [13] it is known, that the confined flow in the wake behind the formation region is stable. That is why we can suggest that 'elliptic instability' type three-dimensional structures in the developed vortex street are induced and 'supported' by perturbed regions generated upstream in the vortex formation region (arrows 3_1–3_4, 4_1–4_4 in Fig. 6a). In the same manner appearance of perturbations in the hyperbolic braid regions can be the reason for the emergence of elliptic-kind instability in the vortex cores of the forming vortices upstream.

4.2. The Evolution of the Perturbed Regions: mode B

4.2.1. Stage I: Perturbations are growing

There is only one interval of linear growth (Fig. 7b). It takes place in the hyperbolic region, where the main vortex is separated from the cylinder (see arrows marked 1_3 and 2_1 in Figs. 6b). The interval of growth ($\approx 0.25\tau$, Fig. 7b) is shorter than for mode A ($\gtrsim 0.5\tau$, Fig. 7a). The scheme in Fig. 6b (row 3) shows that the formed longitudinal vorticity 2_3 is close to the new forming perturbations 1_3 and can influence the spatial structure of these perturbations. It was noticed in [4] and the self-sustained process
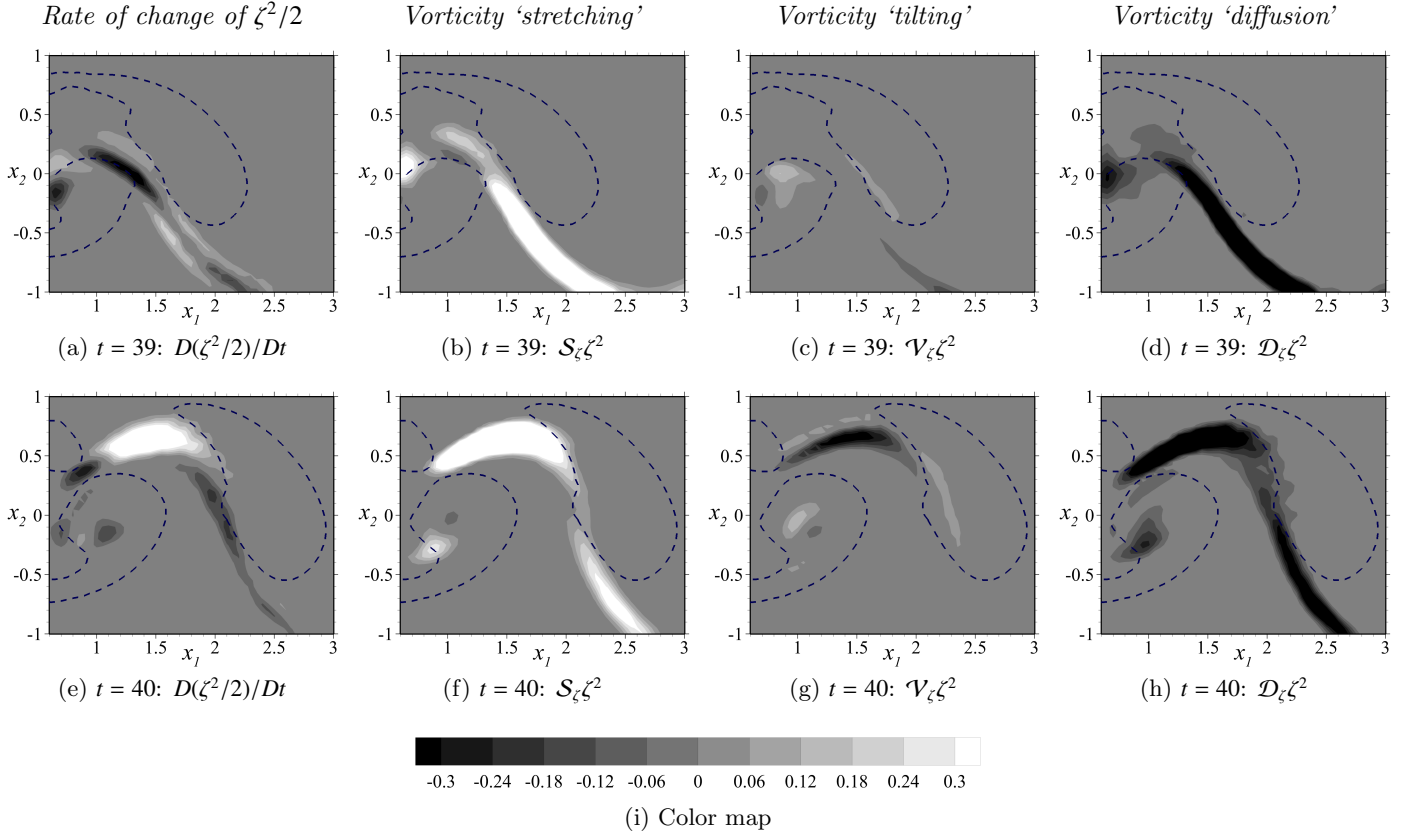
10

Fig. 9: The rate of variation of perturbation amplitude (multiplied by factor ζ) $D\zeta/Dt$ (a, e) in the fluid particle for mode B and the contribution of three mechanisms (multiplied by factor ζ^2): vorticity 'stretching' $\mathcal{S}_\zeta$ (b, f), 'tilting' $\mathcal{V}_\zeta$ (c, g), 'diffusion' $\mathcal{D}_\zeta$ (d, h). Dashed lines are the lines of $Q = 0$. The time corresponds to the second ($t = 39$) and third ($t = 40$) rows on the scheme in Fig. 6b. Limit values on the color map (i) are not the maximum and minimum of functions: function values greater than the upper limit (or less than the lower limit) are filled with one color corresponding to this limit.

was described: how previously formed longitudinal vortices cause emergence of perturbations in the braid shear layer. Figs. 5e-h and 9a, e clearly show that the previously formed perturbed region is transferred upstream to the braid shear layer and it is amplified there. It could also be seen in Fig. 9 that because of the viscous diffusion $\mathcal{D}_\zeta$ the amplitude ζ decreases in fluid particles placed in the upstream part of the perturbed region (see dark regions in Fig. 9a, d and e, h). The stage of growth is repeated each half of the period.

Although the growth of the perturbations of mode A at stage II and mode B occurs during the detachment of the vortex from the body, the sub-regions of the hyperbolic part of the flow and the time intervals of intensive growth differ. Mode A is growing at the initial stages of vortex detachment at $t \approx \text{argmax}|C_L(t)|$ (see points 1_4, 2_2 in Fig. 7a) in the subregion near the boundary with the elliptical part of the vortex. While mode B is growing at $t \gtrsim \text{argmax}|C_L(t)|$ (see points 1_3, 2_1 in Fig. 7b) upstream.

The process of perturbations development is mainly observed outside the elliptic regions (Fig. 5). All the growth is mostly caused by the vortex line stretching mechanism $\mathcal{S}_\zeta$ (Fig. 9). In the upstream part of the perturbed region the rate of amplitude change is negative because of

the action of viscous diffusion, $\mathcal{D}_\zeta$ (Fig. 9d, h), which prevents the growth of perturbations spreading upstream by the reversed flow. However, there is some region of perturbation upstream (see Fig. 5a-h), which is transferred downstream inside the main vortex and fading out. The presence of the secondary region $\zeta > 0$ near the cylinder is caused by the separation of perturbations upstream. The fact that this region exists in the flow during a sufficiently large time interval is associated with the local growth of these perturbations near the cylinder. In Fig. 9c, g one can see, that the destabilizing action of mechanism $\mathcal{V}_\zeta$ is most pronounced inside the elliptic part of the flow, where these perturbations exist. In the process of intensive growth in the hyperbolic region shear deformations of the vortex lines $\mathcal{V}_\zeta$ play a noticeable role in ζ reduction (Fig. 9g).

4.2.2. Stage II: Perturbations are fading out

As a result of stretching in the hyperbolic part of the flow, elongated regions of longitudinal vorticity are formed in the wake (arrows 2_3, 2_4, 3_1–3_4 in Fig. 6b). These regions are fading out, while they are traveling downstream in the formed vortex street, see corresponding points in Fig. 7b. Stabilization of the flow is mostly related to the action of

11

viscous diffusion, $\mathcal{D}_\zeta$ (Fig. 9d, h).

5. Conclusions

The system of equations governing the evolution of small longitudinal perturbations of velocity and vorticity vectors can be interpreted as follows: perturbations change in a fluid particle can be caused by the action of the following four mechanisms (see Eqs. (7) and (8)).

(I) Stretching of the vortex lines of disturbances by the base flow ($\mathcal{S}_\zeta$, $\mathcal{S}_\theta$).

(II) Shear deformations of the vortex lines of the base flow by perturbations ($\mathcal{V}_\zeta$, $\mathcal{V}_\theta$).

(III) Viscous diffusion of perturbations ($\mathcal{D}_\zeta$, $\mathcal{D}_\theta$).

(IV) Solid-state rotation of fluid particles ($\mathcal{R}_\theta$).

This interpretation is used to obtain new details of the transition process by analyzing the impact of each mechanism and distinguishing the regions of the flow, where these mechanisms manifest themselves.

For the considered regimes, the interval of perturbations growth is approximately twice as large for mode A as for mode B. It was shown that modes A and B have two and one stages of perturbations linear growth, respectively. Two stages of growth for mode A are related to the development of perturbations in parts of the flow with different properties. At the first stage perturbations are transferred inside the elliptic region, at the second stage they are entering the hyperbolic region of the braid shear layer. The rate of growth for the second stage is higher. Perturbations of mode B are developed mostly outside the elliptic region.

The main mechanism responsible for the growth of perturbations for both modes is stretching of the vortex lines $\mathcal{S}_\zeta$, which produces a significant impact on the growth rate both in the hyperbolic and elliptic parts of the flow. Shear deformations of the vortex lines of the base flow $\mathcal{V}_\zeta$ are responsible for the initial growth of perturbations inside the forming vortices of the base flow for mode A. However, the conditions for the appearance of these perturbations could be created by the previously formed longitudinal vorticity in the hyperbolic region (and not by the elliptic instability of vortex cores by itself), similar to the process of induction of 'elliptic' instability in the formed vortex street. For mode B term $\mathcal{V}_\zeta$ produces mainly a stabilizing effect. For both modes mechanism $\mathcal{D}_\zeta$ stabilizes the three-dimensional structures, mechanism $\mathcal{R}_\theta$ has influence on the orientation of perturbations in a fluid particle and not on the amplitude (only indirect influence is possible).

The results obtained in the present work can be used in constructing simplified models of the process of transition to three-dimensionality, because it allows to localize the regions of development of instability in time and space, and also to estimate the degree of influence of the terms in the equations before making simplifying assumptions.

The presented approach of transitional mechanisms analysis is not restricted to the wake behind a cylinder and can be applied to other problems on the transition to three-dimensionality. It should be noted that there is a certain difference between this approach of studying linear perturbation development and Floquet analysis. Floquet analysis gives a spectrum describing the behavior of perturbations of a special form. In our approach, we are solving the initial-value problem. As a result, we have the evolution of the linear part of real perturbations. These perturbations theoretically can be described as a linear combination of Floquet modes, but for this purpose it is necessary to know more than only the most unstable one. The present approach also gives an idea of which of the physical mechanisms is responsible for the process of destabilization (or stabilization) of the flow.

Appendix A. The Navier-Stokes equations in primitive variables

The matrices in Eq. (1) take the following form:

$$
A_0 = \frac{1}{(\gamma-1)T}
\begin{pmatrix}
1 & 0 & 0 & 0 & -\frac{p}{T} \\
u_1 & p & 0 & 0 & -\frac{pu_1}{T} \\
u_2 & 0 & p & 0 & -\frac{pu_2}{T} \\
u_3 & 0 & 0 & p & -\frac{pu_3}{T} \\
E & pu_1 & pu_2 & pu_3 & -\frac{pu^2}{2T}
\end{pmatrix},
$$

$$
K_{ij} = \frac{1}{\mathrm{Re}}
\begin{pmatrix}
0 & 0 & 0 & 0 & 0 \\
0 & k_{ij}^{11} & k_{ij}^{12} & k_{ij}^{13} & 0 \\
0 & k_{ij}^{21} & k_{ij}^{22} & k_{ij}^{23} & 0 \\
0 & k_{ij}^{31} & k_{ij}^{32} & k_{ij}^{33} & 0 \\
0 & k_{ij}^{s1}u_s & k_{ij}^{s2}u_s & k_{ij}^{s3}u_s & \frac{\gamma\delta_{ij}}{\mathrm{Pr}}
\end{pmatrix},
$$

$$
A_i = \frac{1}{(\gamma-1)T}
\begin{pmatrix}
u_i & p\delta_{1i} & p\delta_{2i} \\
u_iu_1 & pu_i(1+\delta_{1i}) & pu_1\delta_{2i} \\
u_iu_2 & pu_2\delta_{1i} & pu_i(1+\delta_{2i}) \\
u_iu_3 & pu_3\delta_{1i} & pu_3\delta_{2i} \\
u_iE & pu_1u_i+\delta_{1i}pE & pu_2u_i+\delta_{2i}pE
\end{pmatrix}
$$
$$
\begin{pmatrix}
p\delta_{3i} & -\frac{pu_i}{T} \\
pu_1\delta_{3i} & -\frac{pu_iu_1}{T} \\
pu_2\delta_{3i} & -\frac{pu_iu_2}{T} \\
pu_i(1+\delta_{3i}) & -\frac{pu_iu_3}{T} \\
pu_3u_i+\delta_{3i}pE & -\frac{pu_iu^2}{2T}
\end{pmatrix},
$$

$$
P_i = p\,(0, \delta_{1i}, \delta_{2i}, \delta_{3i}, u_i)^*, \quad R = \rho\,(0, F_1, F_2, F_3, u_iF_i)^*.
$$

Here, $E = T + u^2/2$; $u^2 = u_1^2 + u_2^2 + u_3^2$; $k_{ij}^{pq} = \delta_{pq}\delta_{ij} + \delta_{qi}\delta_{pj} - 2\delta_{pi}\delta_{qj}/3$; δ_{ij} is Kronecker delta.

12

References

[1] C. H. K. Williamson, The existence of two stages in the transition to three-dimensionality of a cylinder wake, Physics of Fluids 31 (11) (1988) 3165–3168. doi:10.1063/1.866925.

[2] D. Barkley, R. D. Henderson, Three-dimensional Floquet stability analysis of the wake of a circular cylinder, Journal of Fluid Mechanics 322 (1996) 215–241. doi:10.1017/S0022112096002777.

[3] C. H. K. Williamson, Vortex dynamics in the cylinder wake, Annual Review of Fluid Mechanics 28 (1) (1996) 477–539. doi:10.1146/annurev.fl.28.010196.002401.

[4] C. H. K. Williamson, Three-dimensional wake transition, Journal of Fluid Mechanics 328 (1996) 345–407. doi:10.1017/S0022112096008750.

[5] R. D. Henderson, Nonlinear dynamics and pattern formation in turbulent wake transition, Journal of Fluid Mechanics 352 (1997) 65–112. doi:10.1017/S0022112097007465.

[6] T. Leweke, C. H. K. Williamson, Three-dimensional instabilities in wake transition, European Journal of Mechanics - B/Fluids 17 (4) (1998) 571–586. doi:10.1016/S0997-7546(98)80012-5.

[7] M. C. Thompson, T. Leweke, C. H. K. Williamson, The physical mechanism of transition in bluff body wakes, Journal of Fluids and Structures 15 (3-4) (2001) 607–616. doi:10.1006/jfls.2000.0369.

[8] M. Brede, H. Eckelmann, D. Rockwell, On secondary vortices in the cylinder wake, Physics of Fluids 8 (8) (1996) 2117–2124. doi:10.1063/1.868986.

[9] K. Ryan, M. C. Thompson, K. Hourigan, Three-dimensional transition in the wake of bluff elongated cylinders, Journal of Fluid Mechanics 538 (2005) 1–29. doi:10.1017/S0022112005005082.

[10] F. Giannetti, S. Camarri, P. Luchini, Structural sensitivity of the secondary instability in the wake of a circular cylinder, Journal of Fluid Mechanics 651 (2010) 319–337. doi:10.1017/S0022112009993946.

[11] M. J. Landman, P. G. Saffman, The three-dimensional instability of strained vortices in a viscous fluid, Physics of Fluids 30 (8) (1987) 2339–2342. doi:10.1063/1.866124.

[12] S. Julien, S. Ortiz, J.-M. Chomaz, Secondary instability mechanisms in the wake of a flat plate, European Journal of Mechanics - B/Fluids 23 (1) (2004) 157–165. doi:10.1016/j.euromechflu.2003.07.001.

[13] D. Barkley, Confined three-dimensional stability analysis of the cylinder wake, Physical Review E 71 (2005) 017301. doi:10.1103/PhysRevE.71.017301.

[14] T. J. R. Hughes, G. Scovazzi, T. E. Tezduyar, Stabilized methods for compressible flows, Journal of Scientific Computing 43 (3) (2010) 343–368. doi:10.1007/s10915-008-9233-5.

[15] A. I. Aleksyuk, V. P. Shkadova, V. Y. Shkadov, Formation, evolution, and decay of a vortex street in the wake of a streamlined body, Moscow University Mechanics Bulletin 67 (3) (2012) 53–61. doi:10.3103/S0027133012030016.

[16] A. I. Aleksyuk, Investigation of the separated flows by the numerical solution of Navier–Stokes equations, Ph.D. thesis, M.V. Lomonosov Moscow State University (2013).

[17] A. I. Aleksyuk, V. P. Shkadova, V. Y. Shkadov, Numerical simulation of three-dimensional instability of flow past a short cylinder, Moscow University Mechanics Bulletin 71 (1) (2016) 1–6. doi:10.3103/S0027133016010015.

[18] A. I. Aleksyuk, A. N. Osiptsov, Direct numerical simulation of energy separation effect in the near wake behind a circular cylinder, International Journal of Heat and Mass Transfer 119 (2018) 665–677. doi:10.1016/j.ijheatmasstransfer.2017.11.133.

[19] R. D. Henderson, Details of the drag curve near the onset of vortex shedding, Physics of Fluids 7 (9) (1995) 2102–2104. doi:10.1063/1.868459.

[20] C.-Y. Wen, C.-Y. Lin, Two-dimensional vortex shedding of a circular cylinder, Physics of Fluids 13 (3) (2001) 557–560. doi:10.1063/1.1338544.

[21] A. D. D. Craik, W. O. Criminale, Evolution of wavelike disturbances in shear flows: A class of exact solutions of the Navier-Stokes equations, Proceedings of the Royal Society A: Mathematical, Physical and Engineering Sciences 406 (1830) (1986) 13–26. doi:10.1098/rspa.1986.0061.

[22] R. T. Pierrehumbert, Universal short-wave instability of two-dimensional eddies in an inviscid fluid, Physical Review Letters 57 (17) (1986) 2157–2159. doi:10.1103/PhysRevLett.57.2157.

[23] B. J. Bayly, Three-dimensional instability of elliptical flow, Physical review letters 57 (17) (1986) 2160–2163. doi:10.1103/PhysRevLett.57.2160.

[24] F. Waleffe, On the three-dimensional instability of strained vortices, Physics of Fluids A: Fluid Dynamics 2 (1) (1990) 76–80. doi:10.1063/1.857682.

[25] R. R. Kerswell, Elliptical instability, Annual Review of Fluid Mechanics 34 (1) (2002) 83–113. doi:10.1146/annurev.fluid.34.081701.171829.